Numerical modelling of dislocations and deformation mechanisms in CaIrO and MgGeO post-perovskites – Comparison with MgSiO post-perovskite

Arnaud Metsue, Philippe Carrez, David Mainprice, Patrick Cordier

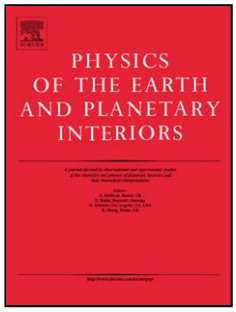

Title: Numerical modelling of dislocations and deformation mechanisms in $CaIrO_3$ and $MgGeO_3$ post-perovskites – Comparison with $MgSiO_3$ post-perovskite

Authors: Arnaud Metsue, Philippe Carrez, David Mainprice, Patrick Cordier

PII: S0031-9201(08)00060-5
DOI: doi:10.1016/j.pepi.2008.04.003
Reference: PEPI 4921

To appear in: *Physics of the Earth and Planetary Interiors*

Received date: 8-10-2007
Revised date: 24-3-2008
Accepted date: 2-4-2008

Please cite this article as: Metsue, A., Carrez, P., Mainprice, D., Cordier, P., Numerical modelling of dislocations and deformation mechanisms in $CaIrO_3$ and $MgGeO_3$ post-perovskites – Comparison with $MgSiO_3$ post-perovskite, *Physics of the Earth and Planetary Interiors* (2007), doi:10.1016/j.pepi.2008.04.003

Numerical modelling of dislocations and deformation mechanisms in $CaIrO_3$ and $MgGeO_3$ post-perovskites – Comparison with $MgSiO_3$ post-perovskite.

Arnaud Metsue [1], Philippe Carrez[1], David Mainprice[2], and Patrick Cordier[1]

[1]Laboratoire de Structure et Propriétés de l'Etat Solide, UMR CNRS 8008, Université des Sciences et Technologies de Lille, 59655 Villeneuve d'Ascq Cedex, France

[2]Géosciences Montpellier UMR CNRS 5243, Université Montpellier 2, 34095 MONTPELLIER Cedex 05, France

Corresponding author:

Patrick CORDIER

Laboratoire de Structure et Propriétés de l'Etat Solide - UMR CNRS 8008

Université des Sciences et Technologies de Lille - Bat C6

59655 Villeneuve d'Ascq Cedex - FRANCE

Phone: (33) 03 20 43 43 41

Fax: (33) 03 20 43 65 91

E-mail: Patrick.Cordier@univ-lille1.fr

Manuscript prepared with Word X on Macintosh

Abstract:

In this study, we propose a theoretical approach to test the validity of the isomechanical analogues for post-perovskite structures. Intrinsic plastic properties are evaluated for three materials exhibiting a post-perovskite phase: $MgSiO_3$, $MgGeO_3$ and $CaIrO_3$. Dislocation properties of each structure are determined using the Peierls-Nabarro model based on first principles calculations of generalised stacking fault and the plastic properties are extended to crystal preferred orientations using a visco-plastic self-consistent method. This study provides intrinsic parameters of plastic deformation such as dislocation structures and Peierls stresses that can be directly compared between the three materials. It appears that it is very difficult to draw any simple conclusions on polycrystalline deformation simply by comparing single crystal properties. In particular, contrasting single crystal properties of $MgSiO_3$ and $CaIrO_3$ lead to similar crystal preferred orientation of the polycrystal aggregates.

Keywords: $CaIrO_3$, $MgSiO_3$, $MgGeO_3$, post-perovskite, deformation mechanisms, dislocations, slip systems, first-principle calculations, Peierls-Nabarro model

Introduction

The lowermost layer of the Earth's mantle, called D", is one of the most important boundary layers of the Earth's interior. This region is characterized by strong heterogeneities and large seismic anomalies (Lay et al., 1998). The recent discovery (Murakami et al., 2004; Oganov and Ono, 2004) (R1-4) that $MgSiO_3$ perovskite transforms into a slightly denser phase (usually called post-perovskite) at ca. 130 GPa, 2000K has provided new insights into the understanding of the D" layer (Oganov and Ono, 2004; Tsuchiya et al., 2004a, b). The layered structure of post-perovskite has been immediately suggested as a possible origin for seismic anisotropy in D". For a strong seismic anisotropy to develop, it is necessary to have a significant elastic anisotropy, but also that the crystal preferred orientation allows this anisotropy to appear at the aggregate level. Knowledge of the active slip systems that produce preferred orientation is thus of primary importance (Oganov et al. 2005, Carrez et al. 2007b).

$MgSiO_3$ post-perovskite cannot be quenched and must be studied *in situ* at high-pressures that can only be attained in a diamond anvil cell (Merkel et al., 2007) (R2). For this reason, the use of analogue materials appears very attractive as it allows more experiments (in particular deformation experiments) to be performed. It is known that orthorhombic $CaIrO_3$ (space group *Cmcm*) is isostructural to $MgSiO_3$ post-perovskite at atmospheric pressure, although at high-temperature, $CaIrO_3$ transforms to a *Pbnm* perovskite phase (Hirose and Fujita, 2005). Over the last fifty years, germanates have been used as low-pressure analogues for silicates. In most cases, the analogy between germanates and silicates have been demonstrated in the studies of phase equilibria and thermodynamics. Indeed, Hirose et al. (2005) have shown recently that $MgGeSiO_3$ exhibits a post-perovskite phase isostructural to $CaIrO_3$ and $MgSiO_3$ pPv at ca. 50 GPa. For this reason, several studies have been carried out recently on $CaIrO_3$ and $MgGeO_3$-pPv (Merkel et al., 2006; Miyajima et al., 2006; Niwa et al., 2007; Walte et al., 2007; Yamazaki et al., 2006) (R2) to infer the plastic behaviour of $MgSiO_3$ at high-pressure. The extension of the analogue approach to rheology and texture development is not straightforward. The first basis for this has been given by (Frost and Ashby, 1982), who have shown that choosing a proper normalization for stress and temperature (usually

stress is normalized to the shear modulus and temperature to the melting temperature although Poirier (1985) emphasizes rightly that this choice is not unique), allows the construction of deformation-mechanism maps. A possible inference from these maps is that under the same normalized conditions, materials belonging to the same isomechanical group would exhibit the same dominant deformation mechanism. Frost and Ashby did not claim detailed comparison of deformation mechanisms, such as slip system activities for instance, in the plasticity field. Keeping that in mind, the recent studies using experimental deformation of $CaIrO_3$ and $MgGeO_3$-pPv to predict texture development in $MgSiO_3$-pPv represent a considerable extension of the isomechanical approach. Indeed, one of the most extensive studies carried out on "isostructural" materials is probably the one performed on perovskites by Poirier and co-workers in the eighties (Beauchesne and Poirier, 1989; Beauchesne and Poirier, 1990; Besson et al., 1996; Poirier et al., 1989; Wright et al., 1992). This study (and others) has shown that the greatest caution must be exercised when comparing the mechanical behaviour of different perovskites. We will show, however in another study that perovskites represent a special case. It is thus important to assess the validity of the concept of isomechanical groups with post-perovskites as far as texture developments are concerned.

We propose here a theoretical approach of this problem. We have shown in several recent studies that the Peierls-Nabarro model combined with first-principle calculations provides a very powerful tool to calculate the dislocation properties of complex oxides (e.g. $SrTiO_3$ perovskite: Ferré et al., 2008) including silicates (Carrez et al., 2006; Carrez et al., 2007a; Carrez et al., 2007b; Durinck et al., 2007a; Ferré et al., 2007). In particular, we have applied this model to $MgSiO_3$-pPv at 120 GPa for which the dislocation core profiles and Peierls stresses (lattice resistance to dislocation glide at 0K) have been calculated (Carrez et al., 2007b). In this study, the same approach is applied to $CaIrO_3$ and $MgGeO_3$-pPv (at 120 GPa). This provides parameters that can be unambiguously compared from one compound to another. With this method we will have the first direct assessment of the intrinsic plastic properties of three isostructural materials.

Computational methods

The Peierls-Nabarro model

This study is based on the Peierls-Nabarro (PN) model combined with first-principle calculation of generalized stacking faults. The method has been described in detail in several recent papers, in particular where we report the results on $MgSiO_3$-pPv (Carrez et al., 2007b). For this reason, the model will not be described here and the reader is invited to refer to Carrez et al. (2007b) to find further information.

Ab initio calculations

Calculations were performed using the *ab initio* total-energy calculation package VASP (Kresse and Furthmüller, 1996a, b). This code is based on the first-principles density functional theory and solves the effective one-electron Hamiltonian involving a functional of the electron density to describe the exchange-correlation potential. Computational efficiency is achieved using a plane wave basis set for the expansion of the single electron wave functions and fast numerical algorithms to perform self-consistent calculations (Kresse and Furthmüller, 1996a). We used the Generalised Gradient Approximation (GGA) derived by Perdew and Wang (1992) and the all-electron Projector Augmented-Wave (PAW) method as implanted in the VASP code (Blöchl, 1994). The outmost core radius for Mg, Ge, Ca, Ir and O are 2, 2.3, 2.3, 2.6 and 1.52 a.u. respectively. For all the calculations, a single cut-off energy of 600 eV was used for the plane-wave expansion (R1-6). The first Brillouin zone is sampled using a Monkhorst-Pack grid (Monkhorst and Pack, 1976) adapted for each supercell geometry in order to achieve the full energy convergence.

The crystallographic structures were optimized (full relaxation of cell parameters and of atomic positions) using a 6×4×4 K-point mesh and the athermal elastic constants were determined as the second order derivative of the energy of a strained equilibrium cell taking into account the pressure effect following Barron and Klein (1965) as explained in Carrez et al. (2006) (R1-7). As $CaIrO_3$ post-perovskite structure is stable at ambient pressure conditions, the calculations were performed under zero external pressure. The calculations of $MgGeO_3$ were carried out under an external pressure of 120 GPa. For all calculations, the convergence energies were below 0.1 meV/atom.

GSF calculations were performed using supercell techniques and relaxation conditions (R1-2) already detailed in Carrez et al. (2007b). Typically, a supercell is built on a Cartesian reference frame defined by the normal to the stacking fault plane and by

the shear direction. The GSF are calculated by imposing a shear displacement to the upper part of the supercell. Five supercells identical to those published in Carrez et al. (2007b) are used in this study to investigate the following slip systems: [100](010), [100](001), [100](011), [001](010), [001](110), [001](100), [010](100), [010](001), ½[110](001) and ½[110]($\bar{1}$10).

Visco-plastic self-consistent (VPSC) model

Crystal preferred orientations were predicted using an anisotropic visco-plastic self-consistent model originally developed by Lebensohn and Tomé (1993). The background of the model and its application to mantle minerals, such as olivine was described in detail by Tommasi et al. (2000) and a recent review of the method is given by Tomé and Lebensohn (2004), thus only a short overview is presented in the following section. The visco-plastic self-consistent approach allows both the microscopic stress and strain rate to differ from the corresponding macroscopic quantities. Strain compatibility and stress equilibrium are ensured at the aggregate scale. At the grain scale, deformation is accommodated by dislocation glide only; other mechanisms such as dynamic recrystallization and grain boundary sliding are not taken into account. The shear rate in a glide system *s* is related to the local deviatoric stress tensor S_{ij} by a viscoplastic law:

$$\dot{\gamma}^s = \dot{\gamma}_0 \left(\frac{\tau_r^s}{\tau_0^s} \right)^{n^s} = \dot{\gamma}_0 \left(\frac{r_{ij}^s S_{ij}}{\tau_0^s} \right)^{n^s}$$

where $\dot{\gamma}_0$ is a reference strain rate and n^s, τ_r^s , and τ_0^s are respectively the stress exponent, the resolved shear stress, and the critical resolved shear stress for the system *s*, whose orientation relative to the macroscopic stress axes is expressed by its Schmid tensor $\mathbf{r}^s$. The potentially active glide systems for post-perovskite structures, their normalized critical resolved shear stresses are evaluated from *ab initio* modelling ; they are presented in Table 8. We used a stress exponent of n=3 for all calculations.

The problem lies in the calculation of a microscopic state (**s,** $\dot{\boldsymbol{\varepsilon}}$) for each grain, whose volume average determines the response of the polycrystal ($\bar{\Sigma}$, $\bar{\mathbf{D}}$). The "1-site" approximation (Molinari et al., 1987) is used in the anisotropic VPSC formulation; the influence of individual neighbouring grains is not taken into account. Interactions

between any individual grain and its surroundings are successively replaced by the interaction between an inclusion with similar crystal orientation and an infinite homogeneous equivalent medium (HEM), whose behaviour is the weighted average of the behaviour of all the other grains. This leads to:

$$\acute{\varepsilon}_{ij} - D_{ij} = -\alpha \tilde{M}_{ijkl}(s_{kl} - \bar{\Sigma}_{kl})$$

where $\tilde{\mathbf{M}}$ is the interaction tensor and α is a constant used to parameterize the interaction between grains and the HEM. α = 0 corresponds to the upper bound homogeneous strain (Taylor) model (see Lebensohn and Tomé (1993)), α = 1 corresponds to the tangent model of Lebensohn and Tomé (1993), and α = infinity to the lower bound stress equilibrium model (Chastel et al., 1993). The VPSC tangent model (α = 1) reproduces all the main features of the CPO previous VPSC studies and has been applied here.

In the models an aggregate of 1000 orientations, initially spherical in shape and randomly oriented, is deformed in simple shear and axial compression. The strain path is imposed by prescribing a constant macroscopic velocity gradient tensor L and a time increment, dt, set to achieve an equivalent strain of 0.025 in each deformation step. The equivalent strain is defined as (Molinari et al., 1987):

$$\varepsilon_{eq} = \int D_{eq}(t)\, dt$$

where the Von Mises equivalent strain rate is:

$$\mathbf{D}_{eq} = \sqrt{2/3 \mathbf{D}_{ij} \mathbf{D}_{ij}}$$

Results

Results of cell parameter and elastic constant are presented in Table 1 and Table 2 for either $MgGeO_3$ or $CaIrO_3$. They are in fairly good agreement with the few available data. As commonly noticed, the discrepancy between values come mostly from the choice of first-principles approximations. The results of GSF calculations are presented in Figure 1 and 2 should be compared to Figure 3 of Carrez et al. (2007b). The GSF is interpreted as follows. In the case of a single peak GSF, it can be characterized to a first order by its maximum value γ^{max}. The most relevant parameter is the maximum restoring force τ^{max} encountered during rigid-body shear of the cell, which corresponds to the maximum

slope of the GSF. Those values are presented in Table 3 for $MgGeO_3$ and $CaIrO_3$. In this Table, τ^{max} is also presented normalized by the corresponding shear modulus (calculated using anisotropic elasticity) to allow easier comparison between different compounds. In some cases, the GSF exhibits a minimum at half-shear between adjacent lattice points. This is important information as it suggests a tendency for perfect dislocations to split into partial dislocations. The separation of the partials is directly constrained by the stacking fault energy (SFE), which is given by the energy value at this minimum. The lower the minimum and hence the SFE, the wider the dislocation core splitting will be. This has strong implications on the mechanical properties as dislocation core spreading usually enhances mobility. Figure 2 presents the GSF corresponding to the three slip systems involving [100] glide that are compared to the previous results obtained on $MgSiO_3$ pPv.

The GSF are used as an input for dislocation core modelling based on the Peierls-Nabarro model. The work presented here follows the results for $MgSiO_3$ pPv (Carrez et al., 2007b) ,where the technique is presented in detail. This description will not be reproduced here. The results of the PN model are summarized in Tables 4 to 7 for $MgGeO_3$ and $CaIrO_3$. In both cases, we have separated results for dissociated and non-dissociated dislocations. In each table, results can be found for both edge and screw dislocations. Figure 3 reproduces some characteristic dislocation core profiles which, should be compared to those calculated in $MgSiO_3$ pPv and correspond to figures 4 to 7 of Carrez et al. (2007b).

Discussion

Dislocation core structures are qualitatively similar in the three compounds. The most striking difference corresponds probably to $1/2[110](1\bar{1}0)$ which is not dissociated in $MgSiO_3$, tends to slightly dissociate in $MgGeO_3$ and is dissociated into three partials in $CaIrO_3$. However, these qualitative differences only reflect some tiny quantitative changes. The greatest contrast between $MgSiO_3$, $MgGeO_3$ and $CaIrO_3$ lies in the relative differences between the mobility of the various dislocations. To assess this property, we use the Peierls stress that probes the intrinsic resistance of the lattice to dislocation glide. This parameter allows straightforward comparison between the three compounds

considered here. To compare the slip systems, we use the following approach. We select for each slip system the highest Peierls stress between edge and screw dislocation segments. This value will be used as a proxy for the critical resolved shear stress (CRSS) since for an expanding dislocation loop, the segment bearing the highest friction will control the deformation rate (see Durinck et al. (2007b) for an illustration based on 3D Dislocation Dynamics in olivine). This allows a comparison of the ease of glide for different slip systems within a given composition. To evaluate the plastic anisotropy of each composition the "CRSS" of a given slip system is divided by the one of the easiest slip system, which is thus scaled to one. The results are presented in Table 8. Our study on $MgSiO_3$ yields the counterintuitive result that $[001](010)$ is the easiest slip system (in the planar core approximation as discussed in Carrez et al. (2007b), a discussion not relevant here as we are just looking for criteria to compare different compounds within the same theoretical approach). We show here that $[001](010)$ is also the easiest slip system for $CaIrO_3$ and among the easiest for $MgGeO_3$ (only 60% harder than the easiest one). However, selecting the easiest slip systems is usually not enough to understand the complexity of plastic deformation of a polycrystal that necessarily involves multiple slip. It is also necessary to consider range of the CRSS values for the individual slip systems. This varies significantly among the three compounds as illustrated on Table 9 or on Figure 2, considering the maximum slope of GSF. There is very little variation in normalized CRSS among slip systems involving [100] glide in $MgSiO_3$. In $MgGeO_3$, [100] glide is 7.1 times harder on (010) than on (001). The opposite is observed with $CaIrO_3$ where [100] glide on (001) is 2.7 times harder than on (010) and variation in CRSS values is much larger. This observation made on a small subset of data has a more general relevance. Table 8 shows that all slip systems for $MgGeO_3$ except [110](110) have normalized CRSS lower than 8. The range of CRSS values of $MgGeO_3$ is very comparable with $MgSiO_3$ for which all slip systems have a CRSS less than 8.4. On the other hand, data appear much more scattered for $CaIrO_3$ for which the maximum ratio is close to 70, 7.5 representing already the ratio between the CRSS of the easiest and the second easiest slip system. From these observations, the most striking difference between $MgSiO_3$, $MgGeO_3$ and $CaIrO_3$ is the exceptional plastic anisotropy of $CaIrO_3$, rather than the comparison of the easiest slip system.

The different mechanical properties exhibited by the three compounds studied here are due to the difference in the bond strengths. It is possible in the post-perovskite structure to evaluate this parameter. Indeed, the layered structure offers the possibility to shear the (010) plane at different levels, which will intersect one or the other bond type. In all the previous calculations, the shear level has been chosen such as to preserve the strongest bonds (Ge-O and Ir-O). To check and quantify this point, we have performed additional calculations of unrelaxed-GSF in $MgSiO_3$, $MgGeO_3$ and $CaIrO_3$ at two different levels. The results are presented in Figure 4. One can see that $CaIrO_3$ exhibits the greatest bond strength contrast. Then comes $MgSiO_3$ and finally $MgGeO_3$ corresponds to the case for which there is the smallest difference between bonds. This is clearly due to the large compression undergone at this pressure. $MgSiO_3$ and $MgGeO_3$ clearly appear very close in terms of bond strength contrast, which is very consistent with their similar degree of plastic anisotropy as shown in Table 8 and compared with $CaIrO_3$ in Table 9.

The real implications of these differences can only be evaluated when slip systems interact during plastic deformation of a polycrystal. To incorporate this aspect, we use our CRSS as an input for a polycrystalline visco-plastic self-consistent (VPSC) model of crystal-preferred orientation development using the CRSS values shown in Table 9. Figure 5 shows the pole figures of all three compositions with post-perovskite structure after a simple shear deformation of 1.73 shear strain or equivalent strain of one. The preferred orientation pattern of $MgSiO_3$ and $CaIrO_3$ are very similar with the highest densities in the [001] pole figure (ca. 3.4 times uniform) near the shear direction and the second highest densities at high angle to the shear plane in the (010), although the (100) has similar density and orientation, indicating [001](010) and [001](100) could be the dominant slip systems. In contrast $MgGeO_3$ has a very different preferred orientation pattern with the highest density in the (001) pole figure at high angle to the shear plane and the second highest density in the [010] close to the shear direction, suggesting [010](001) may be dominant.

The activity of the slip systems (Figure 6) reveals that as expected the percentage of slip on [001](010) is very high for $MgSiO_3$ and $CaIrO_3$ (averaged over the total deformation 35.5% and 43.3% respectively). However, the subsidiary slip systems are very different, for $MgSiO_3$ [001](110) (17.6%) and [100](001) (13.1%) whereas for

$CaIrO_3$ the conjugate systems [100](010) (12.7%) and [010](100) (11.5%) are the most active. In contrast for $MgGeO_3$ the dominant system is [100](001) (31.5%) with subsidiary slip systems [010](001) (21.9%), [010](100) (17.5%) and [001](010) (14.6%). The slip activity shows the dominant activity of [001](010) suggested by the pole figures for $MgSiO_3$ and $CaIrO_3$, but not the activity of [001](100) (1.5% and 1.7% respectively), which in any case has a relatively high CRSS for both compositions. The secondary systems have similar activities, but the systems are different, illustrating the complexity of polycrystalline slip. $MgGeO_3$ is different in two ways, firstly the dominant slip system [100](001) is not the same as $MgSiO_3$ and $CaIrO_3$, and the slip is more evenly distributed among the slip systems reflecting the reduced range in CRSS values. Surprisingly the [001](010) system, which has a low CRSS of 1.6, only has an activity of 14.6% in $MgGeO_3$ placing it below the activity level of the other subsidiary slip systems [010](001) and [010](100) with CRSS of 1.4 and 4.0 respectively. The combined action of [100](001) (31.5%), [010](001) (21.9%) and [010](100) (17.6%) accounts for 71.0% of slip activity, resulting in a preferred orientation that cannot be explained in terms of a dominant single slip system.

Conclusion

Using a predictive modelling approach based on first principles we explore the plasticity of isostructural analogues with the Post-Perovskite structure. Our method permits a clear comparison between the analogues and the silicate, with no adjustable parameters. The first conclusion is that the three compounds considered: $MgSiO_3$ and $MgGeO_3$ at 120 GPa as well as $CaIrO_3$ at 0 GPa exhibit the same dislocation structures with only slight differences in the dislocation core profiles. The main differences arise when dislocation mobilities (assessed from lattice friction through the Peierls stress) are considered. The respective dislocation mobilities do not rank similarly in the three compounds for the slip systems considered. Beyond these considerations, we find that $CaIrO_3$ appears much more anisotropic that the germanate and the silicate. This behaviour is a clear consequence of the bond strengths differences in these materials. Surprisingly, these contrasting single crystal properties do not express themselves in a simple manner when the deformation of the polycrystal is considered. Despite relatively small differences in

CRSS of the two easier glide systems [001](010) in silicate and [100](001) germanate (see Table 9), the easiest slip system plays a critical role and rapidly dominates the texture to formation two completely different CPOs. From this point of view, $CaIrO_3$ develops a CPO remarkably similar to the silicate appears to be an attractive material to model the seismic anisotropy in the core-mantle boundary region.

Acknowledgements

This contribution is made possible through the support by INSU-CNRS (SEDIT programme) and the European Science Foundation (ESF) under the EUROCORES Programme EuroMinScI, through contract No. ERAS-CT-2003-980409 of the European Commission, DG Research, FP6. Computational resources have been provided by IDRIS (project # 031685) and CRI-USTL supported by the Fonds Européens de Développement Régional. The authors wish to thank A. Oganov and F. Heidelbach for careful reviews.

References:

Barron, T.H.K. and Klein, M.L., 1965. Second-order elastic constants of a solid under stress. Proc. Phys. Soc., 85: 523-532.

Beauchesne, S. and Poirier, J.P., 1989. Creep of barium titanate perovskite: a contribution to a systematic approach to the viscosity of the mantle. Phys. Earth Planet. Int., 55: 187-199.

Beauchesne, S. and Poirier, J.P., 1990. In search of a systematics for the viscosity of perovskites: creep of potassium tantalate and niobate. Phys. Earth Planet. Int., 61: 182-198.

Besson, P., Poirier, J.P. and Price, G.D., 1996. Dislocations in $CaTiO_3$ perovskite deformed at high temperature: a transmission electron microscopy study. Phys. Chem. Minerals, 23: 337-344.

Blöchl, P.E., 1994. Projector agmented-wave method. Phys. Rev. B, 50: 17953-17979.

Carrez, P., Cordier, P., Mainprice, D. and Tommasi, A., 2006. Slip systems and plastic shear anisotropy in Mg_2SiO_4 ringwoodite: insights from numerical modelling. Eur. J. Mineral., 18: 149-160.

Carrez, P., Ferré, D. and Cordier, P., 2007a. Implications for plastic flow in the deep mantle from modelling dislocations in $MgSiO_3$ minerals. Nature, 446(7131): 68-70.

Carrez, P., Ferré, D. and Cordier, P., 2007b. Peierls stresses for dislocations in $MgSiO_3$ post-perovskite calculated at 120 GPa from first principles. Phil Mag, 87(22): 1-19.

Chastel, Y., Dawson, P.R., Wenk, H.-R. and Bennett, K., 1993. Anisotropic convection with implications for the upper mantle. J. Geophys. Res., B 98: 17757-71.

Durinck, J., Carrez, P. and Cordier, P., 2007a. Application of the Peierls-Nabarro model to dislocations in forsterite. Eur. J. Mineral. 19: 631-639.

Durinck, J., Devincre, B., Kubin, L. and Cordier, P., 2007b. Mesoscopic simulation of plastic slip in olivine. Amer. Mineralogist, 92: 1346-1357.

Ferré, D., Carrez, P. and Cordier, P., 2007. First-principles determination of dislocations properties of $MgSiO_3$ perovskite at 30 GPa based on the Peierls-Nabarro model. Phys. Earth Planet. Int., 163: 283-291.

Ferré, D., Carrez, P. and Cordier, P., 2008. Modeling dislocation cores in $SrTiO_3$ using the Peierls-Nabarro model. Phys. Rev. B, 77: 014106.

Frost, H.J. and Ashby, M.F., 1982. Deformation-mechanism maps. Pergamon Press, Oxford, 166 pp.

Hirose, K. and Fujita, Y., 2005. Clapeyron slope of the post-perovskite phase transition in CaIrO3. Geophys. Res. Lett., 32: L13313.

Hirose, K., Kawamura, K., Ohishi, Y., Tateno, S. and Sata, N., 2005. Stability and equation of state of $MgGeO_3$ post-perovskite phase. Amer. Mineralogist, 90: 262-265.

Kresse, G. and Furthmüller, J., 1996a. Efficiency of ab-initio total energy calculations for metals and semiconductors using a plane-wave basis set. Comput. Mat. Sci., 6: 15-50.

Kresse, G. and Furthmüller, J., 1996b. Efficient iterative schemes for ab initio total-energy calculations using a plane-wave basis set. Phys. Rev. B, 54: 11169.

Kubo, A. et al., 2006. Stability and equation of state of the post-perovskite phase in $MgGeO_3$ to 2 Mbar. Geophys. Res. Lett., 33: L12S12.

Lay, T., Williams, Q. and Garnero, E.J., 1998. The core-mantle boundary layer and deep earth dynamics. Nature, 392: 461-468.

Lebensohn, R.A. and Tomé, C.N., 1993. A self-consistent anisotropic approach for the simulation of plastic deformation and texture development of polycrystal: application to zirconium alloys. Acta Metall. Mater., 41: 2611-2624.

Merkel, S. et al., 2006. Plastic deformation of $MgGeO_3$ post-perovskite at lower mantle pressures. Science, 311(5761): 644-646.

Merkel, S. et al., 2007. Deformation of $(Mg,Fe)SiO_3$ post-perovskite and D anisotropy. Science, 316(5832): 1729-1732.

Miyajima, N., Ohgushi, K., Ichihara, M. and Yagi, T., 2006. Crystal morphology and dislocation microstructures of $CaIrO_3$: A TEM study of an analogue of the $MgSiO_3$ post-perovskite phase. Geophys. Res. Lett., 33: L12302.

Molinari, A., Canova, G.R. and Azhy, S., 1987. A self-consistent approach of the large deformation crystal polycrystal viscoplasticity. Acta Metall., 35: 2983-2994.

Monkhorst, H.J. and Pack, J.D., 1976. Special points for Brillouin-zone integrations. Phys. Rev. B, 23: 5048-5192.

Murakami, M., Hirose, K., Kawamura, K., Sata, N. and Ohishi, Y., 2004. Post-Perovskite phase transition in $MgSiO_3$. Science, 304(5672): 834-836.

Niwa, K. et al., 2007. Lattice preferred orientation in $CaIrO_3$ perovskite and post-perovskite formed by plastic deformation under pressure. Physics and Chemistry of Minerals, 34: 679-686.

Oganov, A.R., Martonák, R., Laio, A., Raiteri, P. and Parrinello, M., 2005. Anisotropy of Earth's D" layer and stacking faults in the $MgSiO_3$ post-perovskite phase. Nature, 438: 1142-1144.

Oganov, A.R. and Ono, S., 2004. Theoretical and experimental evidence for a post-perovskite phase of $MgSiO_3$ in Earth's D'' layer. Nature, 430: 445-448.

Perdew, J.P. and Wang, Y., 1992. Accurate and simple analytic representation of the electron-gas correlation energy. Phys. Rev. B, 45: 13244-13249.

Poirier, J.P., 1985. Creep of crystals. Cambridge University Press, London, 260 pp.

Poirier, J.P., Beauchesne, S. and Guyot, F., 1989. Deformation mechanisms of crystals with perovskite structure. In: A. Navrotsky and D. Weidner (Editors), Perovskite: a structure of great interest to geophysics and materials science. AGU, Washington DC, pp. 119-123.

Stølen, S. and Trønnes, R.G., 2007. The perovskite to post-perovskite transition in $CaIrO_3$: Clapeyron slope and changes in bulk and shear moduli by density functional theory. Phys. Earth Planet. Int., 164: 50-62.

Tomé, C.N. and Lebensohn, R.A., 2004. Self-consistent homogenization methods for texture and anisotropy. In: D. Raabe, F. Roters, F. Bariat and L.-Q. Chen (Editors), Continuum Scale Simulation of Engineering Materials. Wiley-VCH, Weinheim, pp. 473-497.

Tommasi, A., Mainprice, D., Canova, G. and Chastel, Y., 2000. Viscoplastic self-consistent and equilibrium-based modeling of olivine lattice preferred orientations: Implications for the upper mantle seismic anisotropy. J Geophys Res Solid Earth, 105(B4): 7893-7908.

Tsuchiya, T., Tsuchiya, J., Umemoto, K. and Wentzcovitch, R.M., 2004a. Phase transition in $MgSiO_3$ perovskite in the earth's mantle. Earth Planet. Sci. Lett., 224: 241-248.

Tsuchiya, T., Tsuchiya, J., Umemoto, K. and Wentzcovitch, R.M., 2004b. Elasticity of post-perovskite $MgSiO_3$. Geophys. Res. Lett., 31: L14603.

Walte, N., Heidelbach, F., Miyajima, N. and Frost, D., 2007. Texture development and TEM analysis of deformed $CaIrO_3$: Implications for the D " layer at the core-mantle boundary. Geophys. Res. Lett., 34: L08306.

Wright, K., Price, G.D. and Poirier, J.P., 1992. High-temperature creep of the perovskites $CaTiO_3$ and $NaNbO_3$. Phys. Earth Planet. Int., 74: 9-22.

Yamazaki, D., Yoshino, T., Ohfuji, H., Ando, J.I. and Yoneda, A., 2006. Origin of seismic anisotropy in the D " layer inferred from shear deformation experiments on post-perovskite phase. Earth and Planetary Science Letters, 252(3-4): 372-378.

Tables:

	a (Å)	b (Å)	c (Å)	V (Å^3)
$MgGeO_3$ - This study	2.583	8.316	6.368	136.8
Kubo et al. (2006)	2.557	8.238	6.308	132.9
Hirose et al. (2005)	-	-	-	131.4
$CaIrO_3$ - This study	3.214	9.869	7.332	232.5
Hirose and Fujita (2005)	3.144	9.865	7.297	226.3
Stølen and Trønnes (2007)	3.222	9.849	7.350	233.2

Table 1. Lattice parameters and cell volumes of $MgGeO_3$ (at 120 GPa) and $CaIrO_3$ (at ambient pressure) post-perovskite calculated in this study. Comparison with previous studies is provided.

	C_{11}	C_{22}	C_{33}	C_{44}	C_{55}	C_{66}	C_{12}	C_{13}	C_{23}
$MgGeO_3$ - This study	1128	847	1072	219	151	345	468	376	536
$CaIrO_3$ - This study	371	226	362	58	44	50	90	65	114
$CaIrO_3$ - Stølen and Trønnes (2007)	326	207	355	59	46	61	86	70	122

Table 2. Elastic constants of $MgGeO_3$ (at 120 GPa) and $CaIrO_3$ (at ambient pressure) post-perovskite calculated (GGA) in this study. In case of $CaIrO_3$ comparison is provided with recent results from Stølen and Trønnes. All elastic constants are in GPa.

$MgGeO_3$				
Slip system	γ^{max} ($J.m^{-2}$)	SFE ($J.m^{-2}$)	τ^{max} (GPa)	τ^{max}/μ
[100](010)	5.43	-	70.73	0.21
[100](011)	3.76	-	47.44	0.20
[100](001)	2.67	-	32.51	0.22
1/2[110](001)	13.61	-	107.12	0.51
1/2[110](110)	16.43	16.01	159.48	0.53
[001](100)	9.36	9.28	65.54	0.43
[001](110)	11.63	10.88	119.86	0.77
[001](010)	6.68	4.98	66.97	0.31
[010](100)	17.11	-	85.80	0.25
[010](001)	15.11	2.66	115.62	0.53
$CaIrO_3$				
[100](010)	0.97	-	10.22	0.20
[100](011)	1.55	-	16.10	0.34
[100](001)	1.74	-	18.04	0.41
1/2[110](001)	4.05	-	28.38	0.35
1/2[110](110)	3.27	-	30.10	0.47
[001](100)	3.4	2.56	29.88	0.68
[001](110)	3.4	2.06	30.4	0.67
[001](010)	1.19	0.83	11.05	0.19
[010](100)	4.21	-	22.41	0.45
[010](001)	4.58	1.82	28.68	0.49

Table 3. Results of GSF calculations for $MgGeO_3$ pPv and $CaIrO_3$ pPv. γ^{max} corresponds to the maximum of the GSF curve. In case of camel hump shape, SFE represents the stacking fault energy. τ^{max} is the ideal shear stress and it's normalized to the anisotropic shear modulus.

	Screw					Edge				
	a' (Å)	$Kb/4\pi\tau_{max}$ (Å)	ζ (Å)	ΔW (eV.Å^{-1})	σ_p (GPa)	*a*' (Å)	$Kb/4\pi\tau_{max}$ (Å)	ζ (Å)	ΔW (eV.Å^{-1})	σ_p (GPa)
[100](010)	6.37	0.7	0.9	2.0	121.6	2.58	1.3	1.9	$5\ 10^{-2}$	4.4
[100](011)	10.47	1.0	1.3	2.3	89.9	3.21	1.7	2.2	$1\ 10^{-2}$	0.8
[100](001)	4.185	1.4	1.4	0.3	17.1	1.29	2.2	2.2	$1\ 10^{-4}$	0.01
½[110](001)*	1.29	1.0	1.4	$5\ 10^{-2}$	4.9	4.16	0.9	1.4	2.5	81.3

Table 4: $MgGeO_3$ pPv at 120 GPa. Results of the Peierls-Nabarro model applied to the slip systems [100](010), [100](011), [100](001), ½[110](001) corresponding to non-dissociated dislocations. *a'* is the periodicity of the Peierls valley. $Kb/4\pi\tau^{max}$ corresponds to the half width of dislocation core as defined in the analytical solution of the PN equation whereas ζ is the half width of dislocation core deduced from the numerical solution of the PN equation. ΔW Corresponds to the Peierls energy barrier and σ_p is the calculated Peierls stress needed to overcome the energy barrier.

*In case of the ½[110](001) slip system, values are presented for the following mixed characters: θ = 17° in the "Screw" column and θ = 73° in the "Edge" column (θ is the angle between the Burgers vector and the dislocation line).

	Screw					Edge				
	a' (Å)	ζ (Å)	Δζ (Å)	ΔW (eV.Å^{-1})	σ_p (GPa)	*a*' (Å)	ζ (Å)	Δζ (Å)	ΔW (eV.Å^{-1})	σ_p (GPa)
½[110](110)	6.37	0.5	1.2	6.2	266	4.36	0.8	1.8	3.1	116.6
[001](100)	8.32	1.5	3.7	3.5	48.9	6.37	2.3	7.8	1.1	14.8
[001](110)	4.36	0.5	4	1.4	45.9	6.37	1	7.5	4.2	75.6
[001](010)	2.58	0.8	7.5	0.6	20.1	6.37	1.5	14.5	1.8	27.9
[010](001)	1.29	1.1	24.5	0.1	5.8	4.18	1.1	24.7	1.2	23.9
[010](100)*	6.37	ζ_1=1.7 ζ_2=1.4	6.5	5.3	68.5	8.32	ζ_1=2.4 ζ_2=1.8	9.2	5.3	69.1

*For the [010](100) slip system, the value of ζ are presented for the central dislocation density (ζ_1) and for the outer partials (ζ_2)

Table 5: $MgGeO_3$ pPv at 120 GPa. Results of the Peierls-Nabarro model for dissociated dislocations belonging to slip systems ½[110](110), [001](100), [001](110), [001](010), [010](001) and [010](100). Here, ζ corresponds to the half width of a partial dislocation and Δζ is the equilibrium distance between the two partials.

	Screw					Edge				
	a' (Å)	$Kb/4\pi\tau_{max}$ (Å)	ζ (Å)	ΔW (eV.Å^{-1})	σ_p (GPa)	*a*' (Å)	$Kb/4\pi\tau_{max}$ (Å)	ζ (Å)	ΔW (eV.Å^{-1})	σ_p (GPa)
[100](010)	7.33	1.2	1.6	0.4	10.5	3.21	2.9	4.1	3 10^{-3}	0.2
[100](011)	12.3	0.7	0.5	1.2	61.6	3.21	1.8	1.3	9 10^{-2}	4.4
[100](001)	4.93	0.7	0.5	0.5	28	1.60	1.6	1.5	3 10^{-3}	0.3
½[110](001)	4.93	1.2	2.1	0.8	17.3	1.60	0.9	1.7	3 10^{-2}	1.9

Table 6: $CaIrO_3$ pPv at ambient pressure. Results of the Peierls-Nabarro model applied to the slip systems corresponding to non-dissociated dislocations.

	Screw					Edge				
	a' (Å)	ζ (Å)	Δζ (Å)	ΔW (eV.Å^{-1})	σ_p (GPa)	*a*' (Å)	ζ (Å)	Δζ (Å)	ΔW (eV.Å^{-1})	σ_p (GPa)
½[110](110)*	7.33	ζ_1=1.1 ζ_2=0.6	1.9	1.4	37.8	5.19	ζ_1=1.8 ζ_2=0.8	5.3	0.4	13.7
[001](100)	9.87	0.5	5.2	1.8	53	7.33	1	11.8	0.6	13.8
[001](110)	5.19	0.5	6.2	1.2	35.4	7.33	1	13.7	0.9	12.3
[001](010)	3.21	1.9	16.2	4 10^{-2}	0.9	7.33	4.6	38.8	1 10^{-2}	0.1
[010](001)	1.60	1.3	12.6	1 10^{-2}	0.4	4.93	2.1	20.2	0.6	6.8
[010](100)*	7.33	ζ_1=3.3 ζ_2=0.8	12.8	0.6	9	9.87	ζ_1=11.6 ζ_2=1.2	22.2	1.5	10.9

*For ½[110](110) and [010](100) slip systems, the value of ζ are presented for the central dislocation density (ζ_1) and for the outer partials (ζ_2)

Table 7: $CaIrO_3$ pPv at ambient pressure. Results of the Peierls-Nabarro model applied to the slip systems corresponding to dissociated dislocations.

$MgGeO_3$ at 120 GPa				
Slip system	Peierls stress screw dislocations (GPa)	Peierls stress edge dislocations (GPa)	Maximum Peierls stress (GPa)	Peierls stress normalized to the easiest slip plane
[100](001)	17.1	0.01	17.1	1
[010](001)	5.8	23.9	23.9	1.4
[001](010)	20.1	27.9	27.9	1.6
[001](100)	48.9	14.8	48.9	2.8
[010](100)	68.5	69.1	69.1	4.0
[001](110)	45.9	75.6	75.6	4.4
[110](001)	4.9	81.3	81.3	4.7
[100](011)	89.9	0.8	89.9	5.2
[100](010)	121.6	4.4	121.6	7.1
[110](110)	266.0	116.6	266.0	15.5
$CaIrO_3$ at ambient pressure				
[001](010)	0.9	0.1	0.9	1
[010](001)	0.4	6.8	6.8	7.5
[100](010)	10.5	0.2	10.5	11.6
[010](100)	9	10.9	10.9	12.1
[110](001)	17.3	1.9	17.3	19.2
[100](001)	28	0.3	28	31.1
[001](110)	35.4	12.3	35.4	39.3
[110](110)	37.8	13.7	37.8	42
[001](100)	53	13.8	53	58,9
[100](011)	61.6	4.4	61.6	68.4

Table 8: Summary of the Peierls stresses and comparison of the various slip systems based on the hardest dislocation character. The maximum Peierls stress is the maximum value between the screw and edge characters assuming that the slowest dislocation character will control plastic deformation.

Slip system	$MgSiO_3$	$MgGeO_3$	$CaIrO_3$
[100](010)	4.7	7.1	11.6
[100](001)	2.6	1.0	31.1
[100]{011}	6.8	5.2	68.4
[001](010)	1.0	1.6	1.0
[001]{110}	2.9	4.4	39.3
[001](100)	5.4	2.8	58.9
[010](100)	5.2	4.0	12.1
[010](001)	4.1	1.4	7.5
<110>(001)	4.1	4.7	19.2
<110>{110}	8.8	15.5	42

Table 9: Summary of the CRSS values used for VPSC modelling. Note the hardest system <110>{110} in $MgSiO_3$ and $MgGeO_3$ is different from the hardest system in $CaIrO_3$ [100]{110}.

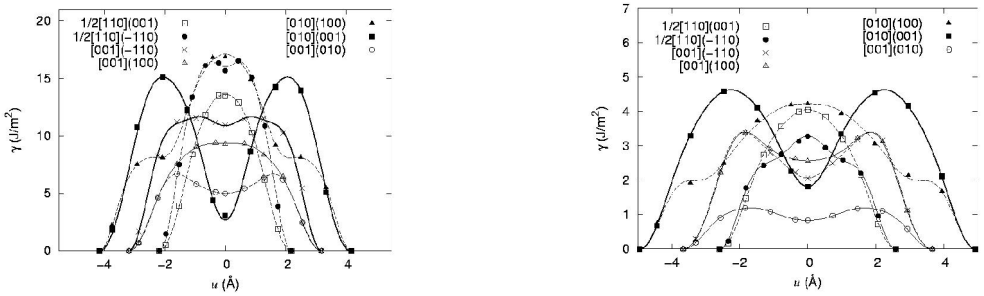

a) b)

Figure 1: Generalized stacking faults calculated in this study (to be compared to Figure 3b of Carrez et al. (2007b) for the case of $MgSiO_3$). The GSFs are displayed against a shear displacement vector *u* rescaled in such a way that *b*/2 shear corresponds to *u*=0 in order to compare the different slip systems.

a) $MgGeO_3$

b) $CaIrO_3$

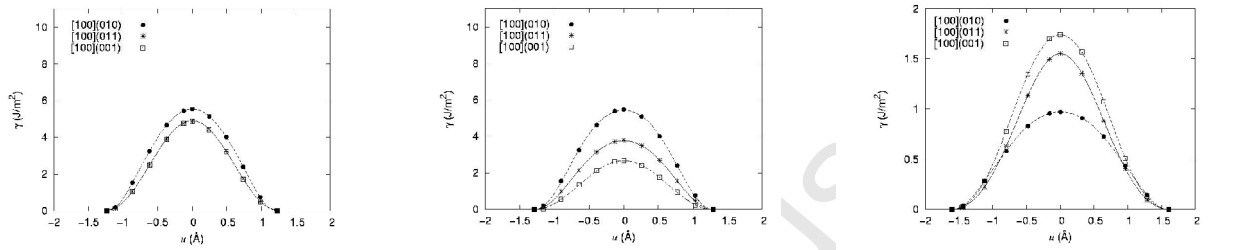

a) b) c)

Figure 2: GSF corresponding to the three slip systems involving [100] glide: $[100](010)$, $[100](001)$ and $[100](011)$. As a guide for the eyes, the GSF of a given slip system, $[100](010)$, has been scaled at the same height in the three graphs. This illustrates the variations among compounds.

a) $MgSiO_3$

b) $MgGeO_3$

c) $CaIrO_3$

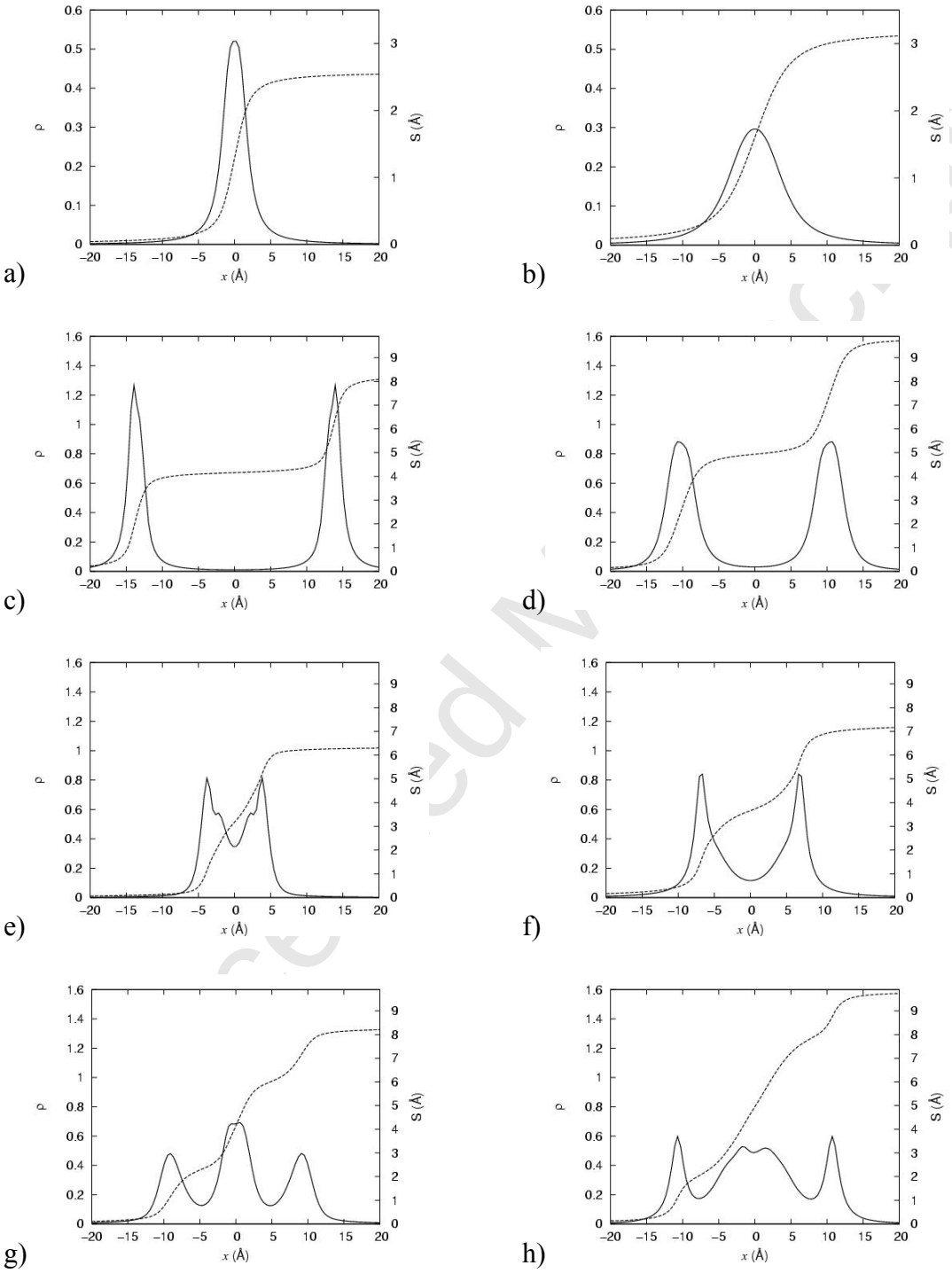

Figure 3: Disregistry, S (dashed line) and dislocation density, ρ, plotted against the distance x of the dislocation core for screw dislocations. Dislocations represented are [100](010), [010](001), [001](110) and [010](100) respectively for $MgGeO_3$ (a, c, e and g) and $CaIrO_3$ (b, d, f and h).

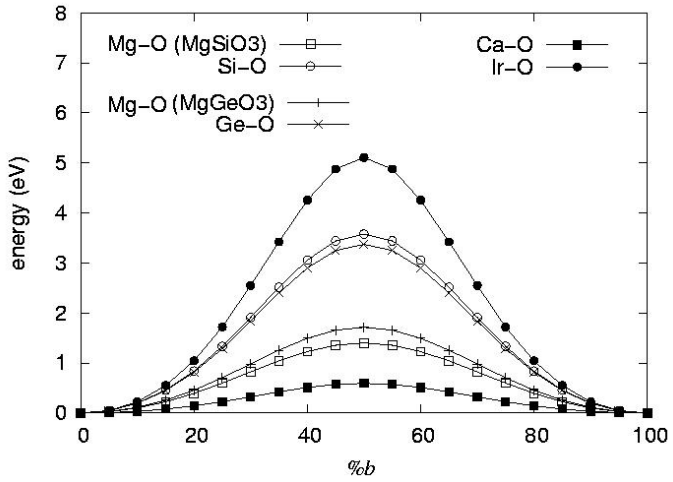

Figure 4: Unrelaxed GSF corresponding to the [100](010) slip system. For each compound, the shear level has been chosen to intersect the octahedral or the hendecahedral layer.

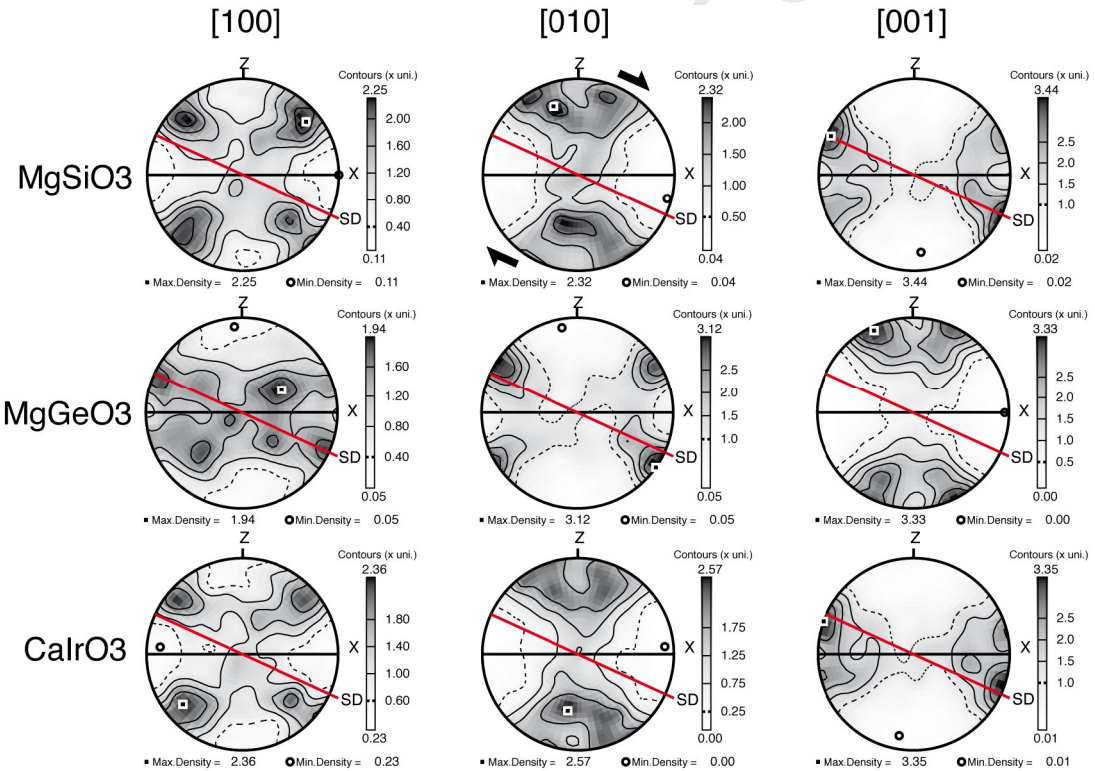

Figure 5: Crystal preferred orientation in simple shear using CRSS predicted by *ab initio* modelling used in VPSC simulation. Shear strain is 1.73 (Equivalent strain 1.0). Finite strain axes are marked X maximum and Z minimum, Horizontal black line is the XY flattening plane. Thick black arrows mark the dextral shear sense, SD is the shear direction and the inclined black line is the shear plane. Lower hemisphere equal area projection.

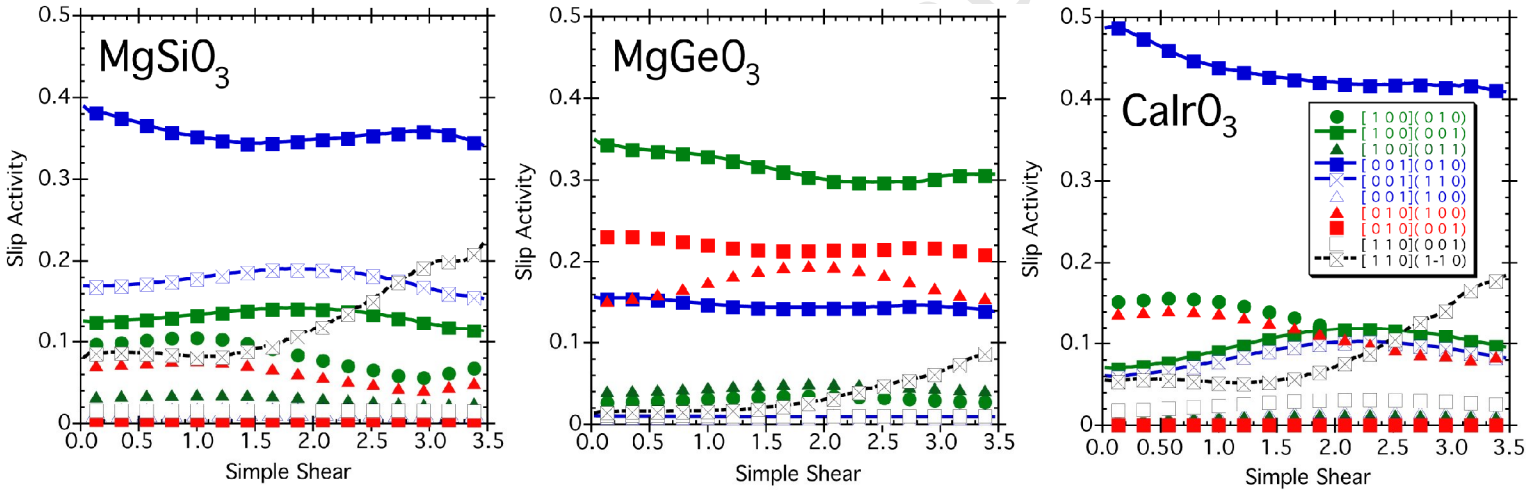

Figure 6: The slip activity in simple shear given by the VPSC simulation. The slip systems the most active in the silicate are indicated by line joining the symbols on all diagram